A Spectral Model of Wind-Forced Internal Waves

DAVID RUBENSTEIN

Science Applications International Corp., McLean, Virginia

(Manuscript received 25 June 1993, in final form 14 September 1993)

ABSTRACT

It is hypothesized that wind forcing is a dominant generator of internal waves. A linear model is derived for the transfer of wind stress into vertical motions associated with internal waves. Two key assumptions are made in order to develop a wavenumber–frequency spectrum of wind stress. The first assumption is that the two-dimensional wavenumber spectrum is separable into two components, one parallel to the direction of mean synoptic flow and the other normal to it. A spectral form for each wavenumber component is hypothesized, based on aircraft measurements of mesoscale wind fields. The second key assumption is that the mesoscale wind field is frozen and advects with a uniform velocity associated with synoptic-scale motions. With these assumptions, the dynamics can be cast into a stationary reference frame—yielding a wavenumber–frequency spectrum—or into a moving reference frame—yielding a 2D wavenumber spectrum.

The resulting internal wave spectrum for vertical velocity is cast into various projections, and compared with the Garrett and Munk spectrum. With the proper choice of model parameters, excellent agreement between frequency spectra is obtained. It is found that the wind stress divergence dominates over wind stress curl in the generation of the internal wave continuum. Various sensitivities to model parameters are explored. A Rayleigh distribution of wind field advection speeds (as observed in synoptic scale weather maps) yields a response very similar to a single, average advection speed (11 m s^{-1}). The lowest vertical mode is the most energetic for conditions where the surface mixed layer depth is greater than about 300 m. For a mixed layer depth of 100 m, the third vertical mode is most energetic.

1. Introduction

Wind forcing is an important generator of near-inertial internal waves. Pollard and Millard (1970), Kundu (1976), and Weller and Halpern (1983) found significant correlation between near-inertial motions in the surface layer and the local wind. Kundu and Thomson (1985) and Rubenstein (1983) showed that linear theory can explain the observed intermittency of near-inertial waves, and the horizontal phase structure of surface-layer oscillations. Gill (1984) presented a linear theory that explained many other features of near-inertial waves, such as the tendency for horizontal and vertical scales to decrease after a storm has passed.

An important question that arises is to what extent can linear dynamics explain the full frequency–wavenumber spectrum of internal waves. Käse (1979) presented a theoretical argument that showed near-inertial wind forcing may be strong enough to maintain the entire internal wave field. Eriksen (1988) examined the linear response of near-inertial waves to a wind stress that deposits a body force as a step function in the vertical; uniformly within a surface layer and zero below. He found that the vertical wavenumber spectral response is the same as that described by the Garrett and Munk GM81 empirical spectrum (Munk 1981).

This agreement between the vertical wavenumber response of a step function wind stress and the GM81 spectrum may simply be fortuitous, or it may reflect wind stress as a dominant source of internal waves. To resolve this question, one needs to look at the full response to a frequency–wavenumber spectrum of the wind stress field. Unfortunately, complete knowledge of the wind field's mesoscale wavenumber–frequency spectrum may remain unknown for a long time. Therefore, the approach used here is to take the best available information about the space–time scales of the wind field and to formulate a hypothetical wavenumber–frequency spectrum. Then the sensitivity of the internal wave response to changes in parameters of the wind stress spectrum can be investigated.

In section 2 a model spectrum of the wind stress field is developed. The basic form of the spectrum is based on aircraft measurements of low-altitude mesoscale winds over the ocean. Two assumptions are made to simplify the spectrum: the wind field is separable in the alongwind and crosswind coordinate directions, and the mesoscale field is frozen and advected with a synoptic pressure system.

In section 3 the basic model equations are presented. The solution is cast as an expansion in terms of normal modes in the vertical. The response function in fre-

Corresponding author address: Dr. David Rubenstein, Science Applications International Corp., 1710 Goodridge Drive, P.O. Box 1303, McLean, VA 22102.

quency, wavenumber, and mode number is derived in terms of the auto- and cross-spectra of wind stress. In section 4 the response spectrum is analyzed. The spectral density of vertical velocity is analyzed in frequency and mode number space. In section 5 the analysis continues in horizontal wavenumber and mode number space. Section 6 presents a summary of results and conclusions.

2. Model spectrum of wind stress

The basic problem in the present approach is that a complete description of the wind stress field or of its power spectrum is not available. Therefore, we make certain simplifying assumptions in order to express the power spectrum in terms of available measurements.

We assume that most of the energetic internal wave spectrum is generated by forcing from the mesoscale wind field. Here we define mesoscale as variability in the length scale range from about 2 to 200 km, corresponding to Orlanski's (1975) β and γ categories. We further assume that mesoscale winds are "frozen" fields that do not evolve with time but are simply advected with the synoptic scale pressure systems and that they are separable in x and y. In equation form, this assumption can be written

$$\frac{\tau^{x,y}(x, y, t)}{\rho} = \tau_0^{x,y} X(x - Ut) Y(y), \qquad (1)$$

where τ^x, τ^y are the components of stress in the x and y directions, ρ is density, and U is the propagation speed of a pressure system. Of course, without wind stress measurements sufficiently sampled in space and time, one cannot directly justify this assumption. We note that the assumption makes the problem tractable. Kundu and Thomson (1985) made a similar assumption in their study of inertial oscillations due to a moving front. D'Asaro (1989) made a slightly less restrictive assumption in his study of inertial oscillations. He did not assume that the wind stress field was separable in x and y but he did make a frozen advection hypothesis:

$$\frac{\tau^{x,y}(x, y, t)}{\rho} = \tau^{x,y}(x - Ut, y, 0). \qquad (2)$$

The amplitude of the propagation speed U is an important parameter for internal waves. To assess the distribution of propagation speeds, we performed a study of the speeds of atmospheric low pressure systems. We used a set of surface level atmospheric pressure analyses of the midlatitudes in the North Atlantic, produced by the Fleet Numerical Oceanographic Center. These analyses were generated at 6-h intervals during the winter of 1976/77. We measured the propagation of low pressure systems and constructed a histogram of propagation speeds. The histogram is shown in Fig. 1, along with an empirical fit of a Rayleigh distribution function. The peak of the distribution function is at 8.8 m s^{-1}, corresponding to a mean propagation speed of $\bar{U} \approx 11$ m s^{-1}.

There have been a number of studies of the time and space scales of wind stress over the ocean. For example, Willebrand (1980) analyzed wind stress over the North Pacific and North Atlantic, and Chave et al. (1991) analyzed the wind stress curl. They used synoptic-scale pressure analyses to compute the quasigeostrophic near-surface winds, which were then transformed to wind stress fields. They found that frequency spectra of wind stress and wind stress curl were nearly flat, or were slightly red for low frequencies. A break in slope to approximately -2 occurs at about 0.2 cycle/day. The smoothing scale for these synoptic analyses is in the range 300–800 km, essentially removing the mesoscale variance. Therefore, these spectral analyses are not useful for describing mesoscales that contribute to wind-forced internal waves.

A description of the spatial scales of the mesoscale wind field is perhaps best obtained from aircraft measurements. Overland and Wilson (1984) analyzed mesoscale variability measured by an aircraft during low-level tracks in directions along and across the mean wind. They analyzed three different mesoscale environments over the ocean. They fitted their measurements to a model of the autocorrelation and cross-correlation functions of the wind. From these correlation functions they derived a model of the power spectrum.

In this paper we assume a wind stress power spectrum of a form similar to that used by Overland and Wilson (1984). We assume that the mean wind is directed parallel to the y direction and that the basic form for the wind stress autospectral density functions for stress in the x and y directions may be written

$$S_\tau^x(k, l)\,dk\,dl = (\tau_0^x)^2 \left(\frac{2}{\pi}\frac{\beta_{xc}}{\beta_{xc}^2 + k^2}\right)\left(\frac{2}{\pi}\frac{\beta_{xa}}{\beta_{xa}^2 + l^2}\right) dk\,dl, \qquad (3)$$

$$S_\tau^y(k, l)\,dk\,dl = (\tau_0^y)^2 \left(\frac{2}{\pi}\frac{\beta_{yc}}{\beta_{yc}^2 + k^2}\right)\left(\frac{2}{\pi}\frac{\beta_{ya}}{\beta_{ya}^2 + l^2}\right) dk\,dl. \qquad (4)$$

Here k and l are wavenumbers in the x and y directions. The terms β_{xc} and β_{xa} are roll-off wavenumbers of the x component of wind stress in the cross- and along-mean wind directions (x and y directions), while the terms β_{yc} and β_{ya} are roll-off wavenumbers of the y component of wind stress in the cross- and along-mean wind directions (x and y directions). We will use the value $\tau^{x,y} = 0.14$ Nt m^{-2} for average stress amplitude. This value was chosen so as to tune model results to be in best agreement with the GM81 spectrum. Moreover, this value is consistent with contour maps of rms stress over the North Atlantic and North Pacific, derived from synoptic analyses by Willebrand (1980).

The forms in parentheses of (3), (4) are similar to that derived by Overland and Wilson (1984) for the spectrum of winds in the along- and across-mean wind direction. They found values for β_a and β_c (corresponding, in their notation to $2m_{ij}$ and $2n_{ij}$) in the range from 0.06 to 0.46 rad km^{-1}, corresponding to wavelengths $\lambda = 2\pi/\beta$ in the range from about 100 to 14 km. Equations (3), (4) do not include a delta-function term derived by Overland and Wilson. This delta-function term represents the variability due to organized mesoscale cloud rolls that were present in one of their analyzed environments. The term is relatively small in amplitude and is not included in this study.

Overland and Wilson (1984) also computed a cross-correlation function between u and v variability, which we can summarize in terms of a cross-spectral density function,

$$S_\tau^{xy}\,dkdl = \tau_0^x\tau_0^y\left(\frac{2}{\pi}\frac{\beta_{xyc}}{\beta_{xyc}^2+k^2}\right)\left(\frac{2}{\pi}\frac{\beta_{xya}}{\beta_{xya}^2+l^2}\right)dkdl. \tag{5}$$

This cross-spectrum will also be needed later in this paper.

3. Basic model equations

We consider three-dimensional geometry with (x, y, z) coordinates corresponding to eastward, northward, and upward directions. The velocity components are u, v, and w. We make the Boussinesq and hydrostatic approximations and write the linearized equations of motion as

$$\frac{\partial u}{\partial t} - fv = -\frac{\partial p}{\partial x} - ru + \frac{\tau^x}{\rho}Z(z) \tag{6}$$

$$\frac{\partial v}{\partial t} + fu = -\frac{\partial p}{\partial y} - rv + \frac{\tau^y}{\rho}Z(z) \tag{7}$$

$$\frac{\partial \rho}{\partial t} - \frac{N^2}{g}w = -r\rho \tag{8}$$

$$\frac{\partial p}{\partial z} + g\rho = 0 \tag{9}$$

$$\frac{\partial u}{\partial x} + \frac{\partial v}{\partial y} + \frac{\partial w}{\partial z} = 0. \tag{10}$$

Here f is the Coriolis parameter, g is the acceleration of gravity, ρ is density perturbation, p is pressure perturbation divided by density, N is the buoyancy frequency, t is time, and r is a damping coefficient. The components (τ^x, τ^y) represent surface stress. The function $Z(z)$ represents the vertical gradient of stress and is distributed uniformly in the surface mixed layer according to the functional form

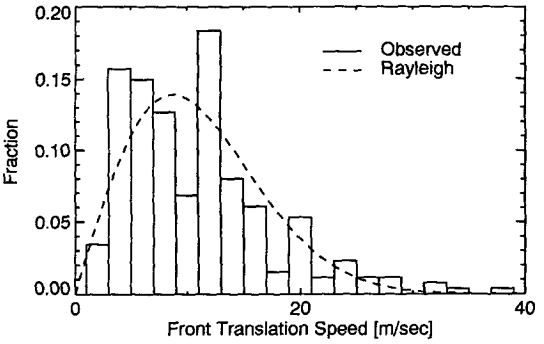

FIG. 1. Histogram of atmospheric front translation speed. Estimates were obtained from synoptic weather charts of the North Atlantic during January and February 1977. The dashed curve shows a Rayleigh density function with a mean value of 11 m s^{-1}.

$$Z(z) = \begin{cases} 0, & 0 < z < D-h \\ 1/h, & D-h < z < D. \end{cases} \tag{11}$$

We define a buoyancy frequency profile to be the same as that of Garrett and Munk (1972),

$$N(z) = \begin{cases} N_0 \exp\left[-\dfrac{(z-(D-h))}{b}\right], & z < D-h, \\ 0, \quad D-h < z < D, \end{cases} \tag{12}$$

where $N_0 = 3$ cph is the surface-extrapolated buoyancy frequency, $b = 1300$ m is a scale depth, and $h = 100$ m is a surface mixed-layer depth. The boundary condition is assumed to be $w = 0$ at the flat bottom and at the surface ($z = 0, D$).

We assume that the mesoscale structure of the wind stress is a frozen field, and that it is simply advected with synoptic-scale weather systems. For simplicity we assume that the wind stress can be written as

$$\tau^{x,y}/\rho = \tau_0^{x,y}(x, y, t). \tag{13}$$

We expand all variables in terms of vertical orthogonal modes;

$$(u, v, p) = \sum_{n=0}^{\infty}(u_n, v_n, p_n)P_n(z), \tag{14}$$

$$(\rho, w) = \sum_{n=0}^{\infty}(\rho_n, w_n)W_n(z). \tag{15}$$

Substituting these relations into (6)–(10) we obtain the vertical structure equation,

$$\frac{d^2W_n}{dz^2} = -\frac{N^2}{c_n^2}W_n, \tag{16}$$

where c_n is a set of eigenvalues. The eigenfunctions $W_n(z)$ and eigenvalues c_n in (16) are solved numeri-

cally. We project the stress distribution function onto a set of vertical modes,

$$Z(z) = \sum_{n=0}^{\infty} \frac{\sigma_n}{c_n^2} P_n(z), \tag{17}$$

and we can solve for the coefficients σ_n in terms of

$$\sigma_n = \frac{\int_0^D W_n'(z)Z(z)dz}{\int_0^D W_n'(z)^2 dz}. \tag{18}$$

We follow the normalization convention used by Eriksen (1988) and require that the integral in the denominator equals D, and then require that

$$\sum_{n=0}^{\infty} \sigma_n^2 = \frac{1}{hD}. \tag{19}$$

Because $W'(z)$ is a constant in the mixed layer, we find that

$$\sigma_n = \frac{1}{D} W_n'(0). \tag{20}$$

We also define the depth average of the squared eigenfunction to be

$$\overline{W_n^2} = \frac{1}{D}\int_0^D W_n(z)^2 dz. \tag{21}$$

We combine (6)–(10) and use (13)–(17) to give

$$\left[\left(\frac{\partial}{\partial t} + r\right)^2 + f^2\right] w_n - c_n^2\left(\frac{\partial^2 w_n}{\partial x^2} + \frac{\partial^2 w_n}{\partial y^2}\right) = \sigma_n\left[f\left(\frac{\partial \tau_0^x}{\partial y} - \frac{\partial \tau_0^y}{\partial x}\right) - \left(\frac{\partial}{\partial t} + r\right)\left(\frac{\partial \tau_0^x}{\partial x} + \frac{\partial \tau_0^y}{\partial y}\right)\right]. \tag{22}$$

Because of our assumption in (1) that the wind stress field propagates with speed U without dispersion, we can choose one of two coordinate systems. We can cast our problem into a stationary coordinate system by replacing ∂_x with $U^{-1}\partial_t$ (as done by D'Asaro 1989), or to a coordinate system moving with the wind field (as done by Kundu and Thomson 1985) by replacing ∂_t with $U\partial_x$. In this section we will consider a transformation to a stationary coordinate system. In section 5 we will consider a transformation to a moving coordinate system.

We replace each occurrence of ∂_x with $U^{-1}\partial_t$ in (22), take the Fourier transform in y and t, and go into frequency–wavenumber space (ω, l) to get a response function $R(\omega, l, n)$ from the left-hand side of (22) as follows:

$$R(\omega, l, n; U) = [f^2 + r^2 - \omega^2(1 - c_n^2/U^2) + c_n^2 l^2 + 2i\omega r]^{-1}. \tag{23}$$

We neglect the r^2 term, as it is very small compared to f^2, and write the squared magnitude of the response function as

$$|R(\omega, l, n; U)|^2 = \{[f^2 - \omega^2(1 - c_n^2/U^2) + c_n^2 l^2]^2 + 4\omega^2 r^2\}^{-1}. \tag{24}$$

Then the power spectral density for w is given by

$$S_w(\omega, l, n; U)d\omega dl = |R(\omega, l, n; U)|^2 \overline{W_n^2}\sigma_n^2 S_F(\omega, l; U)d\omega dl, \tag{25}$$

where $S_F(\omega, l; U)$ is the power spectral density of the forcing term in brackets on the right-hand side of (22). We derive this term as follows: We neglect the term proportional to r, as it is negligible compared to ∂_t. We replace ∂_x with $U^{-1}\partial_t$ in the right-hand side of (22), take the Fourier transform in y and t, and take the magnitude squared, to obtain

$$S_F(\omega, l; U)d\omega dl = \left\{f^2\left[l^2 S_\tau^x\left(\frac{\omega}{U}, l\right) + \frac{\omega^2}{U^2} S_\tau^y\left(\frac{\omega}{U}, l\right) - \frac{2l\omega}{U} S_\tau^{xy}\left(\frac{\omega}{U}, l\right)\right]\right. \quad \begin{matrix}[1] \\ \end{matrix} \quad \begin{matrix}[2] \\ \end{matrix} \quad \begin{matrix}[3] \\ \end{matrix}$$

$$\left. + \left[\frac{\omega^4}{U^2} S_\tau^x\left(\frac{\omega}{U}, l\right) + \omega^2 l^2 S_\tau^y\left(\frac{\omega}{U}, l\right) + \frac{2\omega^3 l}{U} S_\tau^{xy}\left(\frac{\omega}{U}, l\right)\right]\right\} \frac{d\omega}{U} dl. \tag{26}$$

$$[4] \qquad [5] \qquad [6]$$

The terms in (26) are labeled [1–6], for reference in our analyses. Terms [1–3] refer to the curl of the wind stress, and terms [4–6] refer to the rate of change of the wind stress divergence. Terms [1], [2], [4], and [5] are autospectra given by (3) and (4). Terms [3] and [6] are cross spectra given by (5).

4. Model analysis: Frequency-mode spectrum

We begin our analysis by recognizing that the response function $R(\omega, l, n; U)$ given in (23) and (24) represents the impulse response function of a damped harmonic oscillator. For a particular wavenumber component l, vertical mode n, and propagation velocity U, the resonance frequency is given by

$$\omega_{\text{res}}^2 = \omega_0^2 - \frac{2r^2}{(1 - c_n^2/U^2)^2}, \quad (27)$$

where ω_0^2 is the resonance frequency in the absence of damping and is given by

$$\omega_0^2 = \frac{f^2 + c_n^2 l^2}{1 - c_n^2/U^2}. \quad (28)$$

The amplitude damping term may be written $r = (2T_{\text{diss}})^{-1}$, where T_{diss} is an energy dissipation time scale. Here T_{diss} represents the time required for dissipation to drain the internal wave field of energy in the absence of forcing (see, e.g., Garrett 1991; Gregg et al. 1986; Gregg 1984). Typical estimates for T_{diss} range from 30 to 100 days; we will assume a value of 45 days corresponding to $r = (90 \text{ days})^{-1}$. The Q factor of the oscillator is then given by

$$Q = \frac{\omega_{\text{res}}}{2r}(1 - c_n^2/U^2) \sim \frac{f}{2r} \sim \text{O}(400). \quad (29)$$

This value for the Q factor corresponds to a rather weakly damped oscillator.

The spectral density for vertical velocity can be computed from (25) and (26) with reference to (3)–(5). The spectral density is plotted in Fig. 2, for parameter values $r = (90 \text{ days})^{-1}$, $U = \bar{U} = 11 \text{ m s}^{-1}$, and for the two values $l = 2\pi/(15 \text{ km})$ and $2\pi/(150 \text{ km})$. Only term [5] from (26) is included here, as we will show later that this term dominates most of the spectrum. In these plots, the first three individual vertical modes are shown, as well as the sum over the first 20 modes. Each mode shows an individual resonance, given by (27). At high frequencies, well above ω_{res}, the slope of the spectral density for individual modes asymptotes to -2. This slope represents a combination of the -4 slope in the squared response function $|R|^2$ in (24) and the $+2$ slope from term [5] in (26).

We note that this -2 asymptotic slope in the vertical velocity spectrum is equivalent to a -4 slope in a vertical displacement spectrum. These slopes are in contrast with the GM spectrum, which describes a 0 slope in vertical velocity and a -2 slope in displacement. However, the ocean is not forced at a single horizontal wavenumber, but over a continuous spectrum. We apply this continuous spectrum by performing the integration,

$$S_w(\omega, n; U) = \int_0^\infty S_w(\omega, l, n; U) dl, \quad (30)$$

and a summation over the first 20 modes,

$$S_w(\omega; U) = \sum_{n=1}^{20} \int_0^\infty S_w(\omega, l, n; U) dl. \quad (31)$$

Figure 3 shows the frequency dependence of $S_w(\omega; \bar{U})$; the components associated with each of the six individual forcing terms in (26) and the subtotals over the first three and the last three terms are shown. Here the spectral density is expressed in units of $(\text{m s}^{-1})^2(\text{rad s}^{-1})^{-1}$, and is plotted as a function of cycles per hour (cph). Terms [1] and [5] dominate the subtotals, as they include a proportionality to l^2. The important point to notice is that the spectra are rather smooth functions; by integrating over all wavenumbers, a continuum of resonances is combined, resulting in smooth functions of frequency.

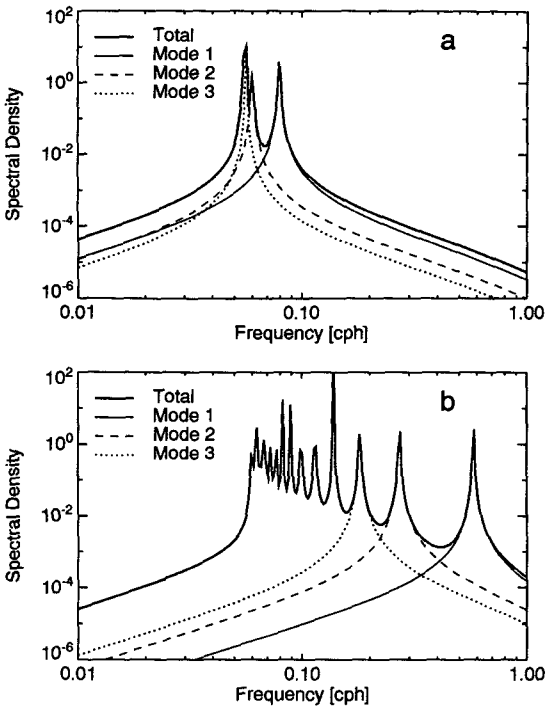

FIG. 2. Spectral density of vertical velocity, in units of $(\text{m s}^{-1})^2(\text{rad s}^{-1})^{-1}$, for parameter values (a) $l = 2\pi/(150 \text{ km})$ and (b) $l = 2\pi/(15 \text{ km})$. The total spectral density is shown (thick solid) as well as the explicit contributions by the first three modes. The sharp spikes correspond to frequency resonances associated with particular mode–wavenumber combinations.

The dominant terms [1] and [5], and the sum over all six terms are shown in Fig. 4. The spectral density $S_w(\omega, n; \bar{U})$ is shown for the first 8 modes; $n = 1, 2, \cdots, 8$, as well as the summation over the first 20 modes, $S_w(\omega; \bar{U})$. While the modal summation of term [1] (Fig. 4a) has approximately a -2 slope in frequency, term [5] (Fig. 4b) has approximately a 0 slope. As a result, term [5] dominates over most of the internal wave frequency band; the sum over all six terms (Fig. 4c) is very similar in shape to that of term [5].

Figure 5 shows a comparison between the total spectral density and the GM spectrum. The wind-forced model agrees well in shape and amplitude with the GM spectrum. Figure 6 shows a comparison between the spectral density $S_w(\omega, n; \bar{U})$ and the corresponding GM spectrum. While the shapes are similar, we note that unlike the GM spectrum, the wind-forced spec-

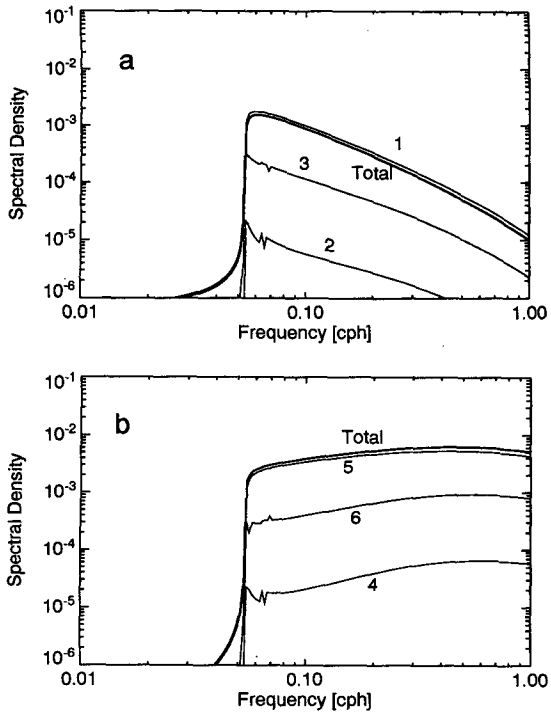

FIG. 3. Wind-forced model spectral density of vertical velocity, in units of $(\mathrm{m\ s^{-1}})^2(\mathrm{rad\ s^{-1}})^{-1}$. Wind stress curl terms [1–3] are shown in (a), and wind stress divergence terms [4–6] are shown in (b). Sharp resonances seen in Fig. 2 have been smoothed out through integration with respect to horizontal wavenumber l.

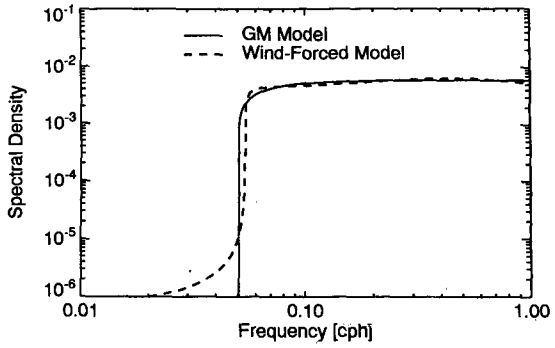

FIG. 5. Comparison between wind-forced model and GM81 model of spectral density of vertical velocity, in units of $(\mathrm{m\ s^{-1}})^2(\mathrm{rad\ s^{-1}})^{-1}$.

trum is not separable in ω and n. The lowest few modes contribute variance to the vertical velocity spectrum preferentially at high frequencies ($\omega \gg f$), while the higher modes contribute preferentially at low, near-inertial frequencies ($\omega \sim f$). This result can also be seen in Fig. 4c.

The spectral density of vertical velocity, $S_w(\omega, n; U)$ can be converted into a spectral density of total energy (= kinetic + potential) through the approximate formula

$$S_e(\omega, n; U) \approx \frac{N^2 f^2}{2(\omega^2 - f^2)\omega^2} S_w(\omega, n; U). \quad (32)$$

The fraction of energy in a given mode is then given by

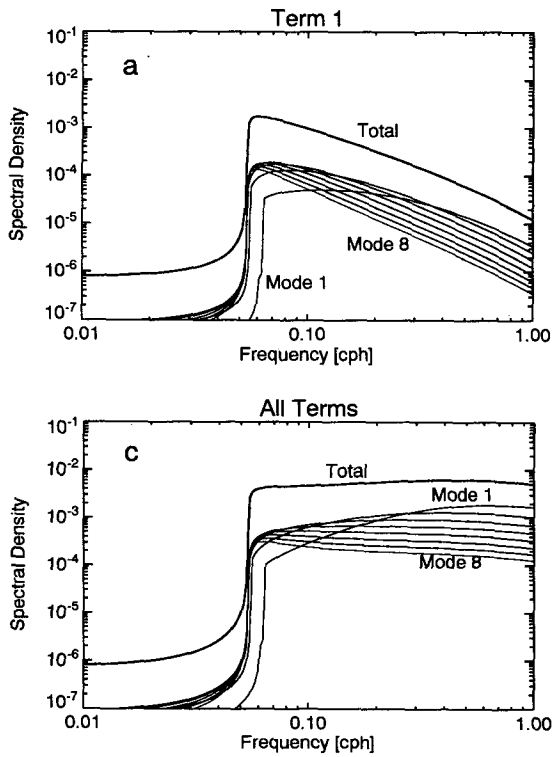

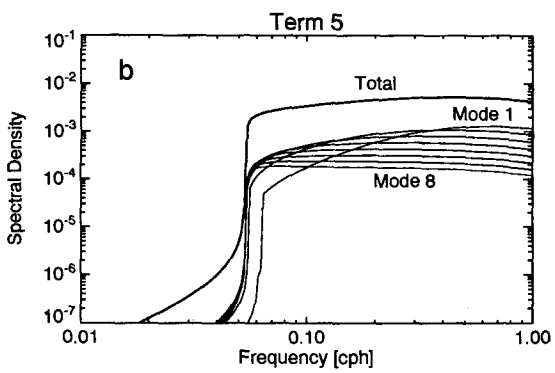

FIG. 4. Wind-forced model spectral density of vertical velocity, in units of $(\mathrm{m\ s^{-1}})^2(\mathrm{rad\ s^{-1}})^{-1}$. Wind stress curl term [1] is shown in (a), wind stress divergence term [5] in (b), and the sum of all terms [1–6] in (c). The total spectral density, as well as explicit contributions by the first eight modes are shown. Sharp resonances seen in Fig. 2 have been smoothed out through integration with respect to horizontal wavenumber l.

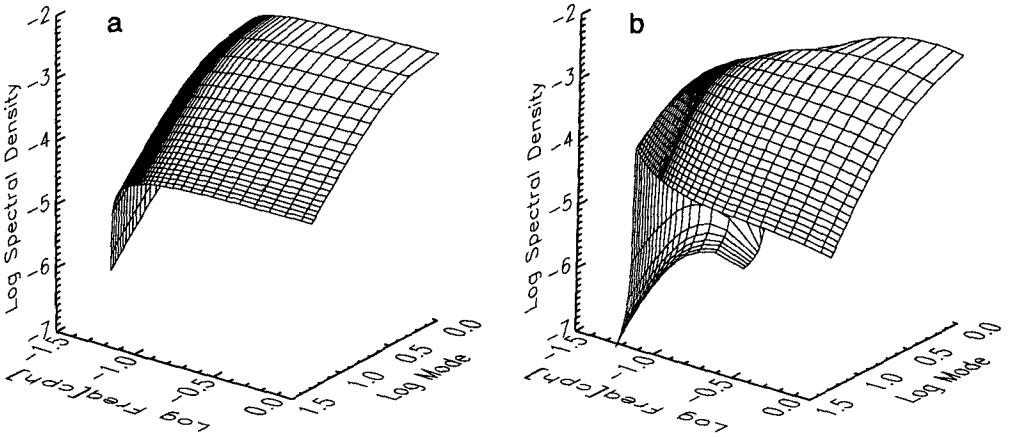

FIG. 6. Comparison between (a) GM81 model and (b) wind-forced model of spectral density of vertical velocity as a function of frequency and vertical mode number.

$$F_e(n; U) = \frac{\int_f^N S_e(\omega, n, U)d\omega}{\sum_n \int_f^N S_e(\omega, n, U)d\omega}. \quad (33)$$

Figure 7 shows a comparison between the fraction of energy $F_e(n) = F_e(n; U = \bar{U})$, the GM modal distribution of energy $H(n)$ given in (A.4), and the energy fraction of the baroclinic modes far from resonance, $hD\sigma_n^2$, for $h = 100$ m, $D = 5$ km ($h/D = 0.02$). Eriksen (1988) found excellent agreement between $hD\sigma_n^2$ [in his notation, $h/D \cdot G_n'(0)^2$] and $H(n)$, particularly for h/D in the range 0.02 to 0.04. Both energy distributions $H(n)$ and $hD\sigma_n^2$ decay monotonically with mode number n. In contrast, the wind-forced energy distribution $F_e(n)$ is peaked at $n = 3$.

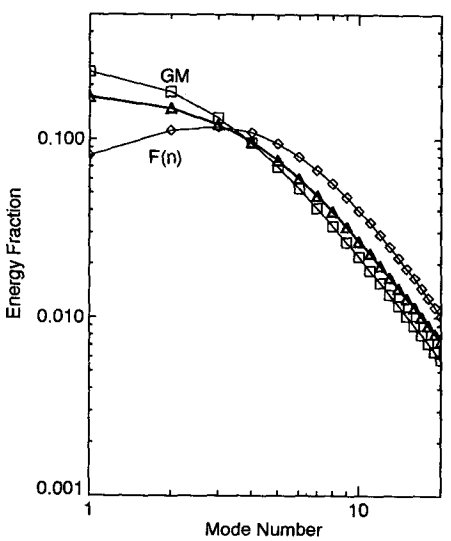

FIG. 7. Fraction of total internal wave energy given by wind-forced model (diamonds), by the GM81 model (squares), and by a baroclinic mode model far from resonance (triangles) from Eriksen (1988) for $h/D = 0.02$.

At this point we can explore the sensitivity of the wind-forced model to various parameters. Figure 8a shows the sensitivity of the energy fraction $F_e(n)$ to variations in the mixed layer depth, h. As the mixed layer deepens, lower modes are emphasized. Shallow mixed layers ($h \leq 200$ m) show a distinct peak at low modes, while a deep mixed layer ($h \geq 400$ m) shows a monotonic decrease in energy distribution, as a function of mode number.

This behavior is consistent with observations. Sanford (1991) and Eriksen (1988) resolved internal wave velocity profiles onto sets of normal modes. In midlatitudes, both investigators observed peaks in energy density in mode $n = 3$. In the wind-forced model, this result translates to a mixed layer depth $h \approx 100$ m.

Figure 8b shows the spectral density is inversely proportional to h; Eriksen (1988) also described this inverse proportionality. In addition, Fig. 8b shows that higher frequencies are slightly emphasized as the mixed layer deepens.

Figure 9 shows how the spectral density $S_w(\omega; \bar{U})$ depends on the damping coefficient r for three values: $r = (45 \text{ days})^{-1}$, $(90 \text{ days})^{-1}$, and $(180 \text{ days})^{-1}$. The amplitude of spectral density in the internal wave band varies as r^{-1}, while the shape of the spectral density does not vary significantly.

Figure 10 shows how the spectral density varies as a function of front translation speed, U. Spectra for values $U = 4$, 10, and 20 m s^{-1} are shown. In addition, a composite spectrum that has been weighted according to the Rayleigh distribution of translation speed, mentioned in section 2, is shown, where the average translation speed is $\bar{U} = 11$ m s^{-1}. The Rayleigh distribution is very similar to the spectral density corresponding to $U = 10$ m s^{-1}. The spectral density is approximately inversely proportional to U. The shape of the spectrum is not sensitive to U at low frequencies, ($\omega \leq 0.3$ cph),

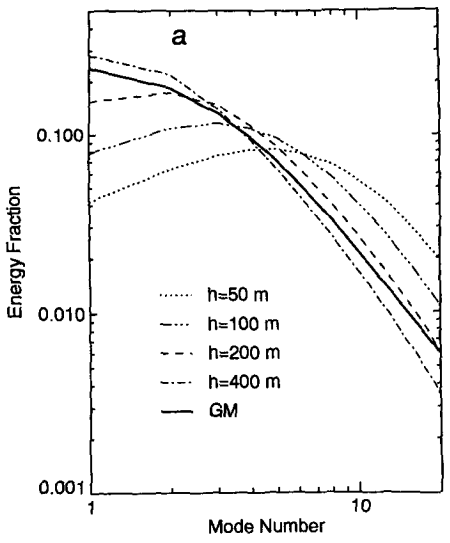

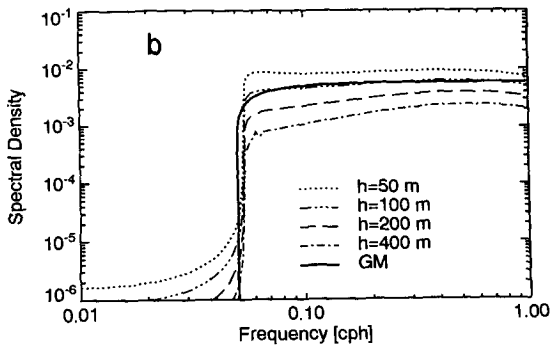

FIG. 8. (a) Sensitivity of energy fraction to variation in mixed layer depth h, compared with GM81 model, as a function of vertical mode number. (b) Sensitivity of spectral density of vertical velocity to variation in mixed layer depth h, compared with GM81 model, as a function of frequency.

but is slightly dependent on U at higher frequencies ($\omega > 0.3$ cph).

The reason for the inverse proportionality between spectral density and front translation speed, U, arises from our transformation to a stationary coordinate system. Consider a small-scale feature in the wind stress field. When this feature is advected past a fixed point with translation speed U, it is observed as a short timescale perturbation. The duration of this perturbation is inversely proportional to U. The frequency bandwidth associated with the perturbation increases with U. As energy is conserved, the spectral density must be inversely proportional to U.

There are six different roll-off wavenumbers β in (3), (4), and (5). Rather than explore the sensitivity to all combinations of variation between the β components, we will instead consider only a few cases, where $\beta_c \equiv \beta_{xc} = \beta_{yc} = \beta_{xyc}$ and $\beta_a \equiv \beta_{xa} = \beta_{ya} = \beta_{xya}$.

Figure 11a shows three curves, corresponding to roll-off wavenumbers $\beta_c = \beta_a = 2\pi/\lambda$, for $\lambda = 15$, 30, and 60 km. Total energy is insensitive to the value of β, although high (low) frequencies are somewhat emphasized by high (low) values of β. Figure 11b shows four curves, corresponding to $(\beta_c, \beta_a) = (2\pi/\lambda_c, 2\pi/\lambda_a)$, for $(\lambda_c, \lambda_a) = (15, 60), (15, 15), (60, 60)$, and $(60, 15)$ km. We see that variation in the crosswind roll-off wavenumber serves mainly to change the overall spectral level, while variation in the alongwind roll-off wavenumber slightly changes the spectral slope.

5. Model analysis: Horizontal wavenumber–mode spectrum

In this section we transform the model equations to a coordinate system moving with the wind field. We do this by replacing ∂_t by $U\partial_x$ in (22). Then (24)–(26) are replaced with

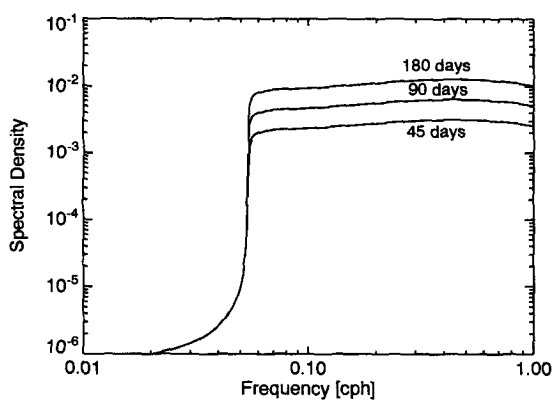

FIG. 9. Sensitivity of wind-forced spectral density model of vertical velocity to variations in damping coefficient, r.

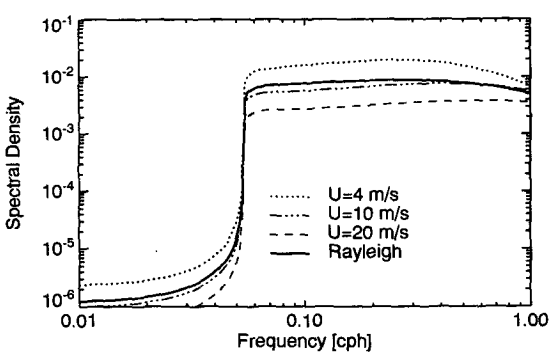

FIG. 10. Sensitivity of wind-forced spectral density model of vertical velocity to variations in front translation speed, compared with a Rayleigh distribution of translation speeds.

$$|R(k, l, n; U)|^2 = \{[f^2 + c_n^2(k^2 + l^2) - k^2U^2]^2 + 4k^2U^2r^2\}^{-1}, \quad (34)$$

$$S_w(k, l, n; U)dkdl = |R(k, l, n; U)|^2\overline{W_n^2}\sigma_n^2 S_F(k, l; U)dkdl, \quad (35)$$

where the wind-forcing spectrum is given by

$$S_F(k, l; U)dkdl = \{f^2[l^2 S_\tau^x(k, l) + k^2 S_\tau^y(k, l) - 2klS_\tau^{xy}(k, l)] + k^2U^2[k^2 S_\tau^x(k, l) + l^2 S_\tau^y(k, l) + 2klS_\tau^{xy}(k, l)]\}dkdl. \quad (36)$$

[1] [2] [3] [4] [5] [6]

If we were to integrate (35) with respect to dl, then we would obtain the same results as in section 4, if we had replaced all occurrences of ω with kU in (24)–(26). To obtain results from an independent dimension, we integrate (35) with respect to horizontal wavenumber component k to give

$$S_w(l, n; U) = \int_0^{k_{max}} S_w(k, l, n; U)dk. \quad (37)$$

Rather than taking the upper limit of this integral to be infinity, we take the upper limit to be $k_{max} = N/U$. This limit results if we do not allow frequencies greater than the buoyancy frequency, N.

The GM spectrum is shown in Figs. 12a and 12b. Figure 12a shows $S_w^{GM}(\alpha, n)$ given in (A6), where $\alpha = (k^2 + l^2)^{1/2}$ is the total horizontal wavenumber magnitude. Note that this spectrum is not separable in α and n. To form a valid comparison between the GM spectrum and the wind-forced spectrum, we convert the GM spectrum from an expression in total horizontal wavenumber $S_w^{GM}(\alpha, n)$ to one in a single wavenumber component, $S_w^{GM}(l, n)$, given in (A9) and shown in Fig. 12b. In contrast to $S_w^{GM}(\alpha, n)$, we see that $S_w^{GM}(l, n)$ does appear to be almost separable in l and n, except in the region of large l and small n. This region of the spectrum drops off because of the cutoff $\alpha_{max} = n\pi/b$ of the upper limit in the integral (A8).

Figures 12c and 12d show $S_w(l, n; U)$ evaluated through the integral in (37), using all six forcing terms in (36). The parameters used here are $U = 11$ m s^{-1}, $h = 25$ m, and $r = 1/(10$ days$)$; $(\beta_c, \beta_a) = (2\pi/\lambda_c, 2\pi/\lambda_a)$ with $(\lambda_c, \lambda_a) = (60, 30)$ km for Fig. 12c and $(\lambda_c, \lambda_a) = (90, 10)$ km for Fig. 12d. These parameters were chosen to allow Fig. 12d to give the best agreement with the GM spectrum in Fig. 12b. The contrast between Figs. 12c and 12d give one a feeling for the rather weak sensitivity to changes in the roll-off wavenumbers (β_c, β_a).

It is interesting to note that the GM spectrum and the wind-forced model spectrum, shown in Figs. 12c and 12d, exhibit similar cutoffs in the region of large l and small n. The cutoff in the GM spectrum arises from the upper limit $\alpha_{max} = n\pi/b$ in the integral (A8). The cutoff in the wind-induced model spectrum follows from the upper limit $k_{max} = N/U$ in the integral (37). These two integrals are not exactly analogous. Their respective upper limits are also not exactly analogous, as the upper limit α_{max} arises from the dispersion relation for internal waves (A5), while the upper limit k_{max} arises from the dispersion relation for the frozen field advection of the wind forcing, $\omega = Uk$. However, both cutoffs follow from asserting an upper frequency limit, $\omega_{max} = N$.

The availability of six roll-off wavenumber parameters might provide sufficient degrees of freedom to tune the wind-forced model over a very wide range of "observational spectra." However, our self-imposed constraints $\beta_c \equiv \beta_{xc} = \beta_{yc} = \beta_{xyc}$ and $\beta_a \equiv \beta_{xa} = \beta_{ya} = \beta_{xya}$ restrict our tuning to two parameters.

6. Conclusions and discussion

In this paper, the spectral response of vertical velocity due to wind-forced internal waves was derived. We summarize with the following conclusions:

1) The linear response of the ocean to surface wind stress may be sufficient to explain much of the total energy of the internal wave field, as well as the distribution of space and time scales. For certain ranges of wind stress model spectrum parameters, there is good agreement with the GM81 empirical spectrum.

2) The internal wave responses to wind stress divergence and wind stress curl are roughly comparable in the near-inertial frequency band. In the internal wave continuum at higher frequencies, wind stress divergence dominates.

3) For a mixed layer depth of 100 m, the third vertical mode is the strongest contributor to the total internal wave energy.

4) The spectral density of vertical velocity as a function of frequency is inversely proportional to front translation speed. Here, it is important to note the assumption that the mesoscale wind stress field is advected with a uniform speed as frozen turbulence.

5) The frequency–vertical wavenumber spectrum is not separable, in contrast to the GM81 model.

6) The slope of the frequency spectrum becomes more blue with increasing roll-off wavenumber in the hypothesized wind stress power spectrum.

The spectral model of internal waves is derived in terms of the spectrum of the wind stress field. This spectrum is not well known. Nevertheless, the wind-forced internal wave model agrees well with the GM81 empirical spectrum, over certain ranges of model parameters. The agreement is not perfect in all details, and adjusting model parameters (h, β_a, β_c) will not necessarily improve the agreement. There are several reasons for this:

1) The assumed form of the wind stress spectrum might not be correct. In particular, the separability of the 2D spectrum into components in the cross- and along-mean wind directions is open to question.
2) There are other important sources of internal wave energy that have been neglected, such as the generation of internal tides.
3) Dynamical effects such as the interaction of internal waves with mesoscale structure, the β effect, and irregular bathymetry have been neglected.
4) There are strong nonlinear mechanisms that transfer energy from one part of the spectrum to another. These mechanisms eventually lead to energy dissipation. These mechanisms are parameterized by the damping coefficient r in the present wind-forced model.

Frequency spectra are computed up to a maximum frequency of 1 cph. As discussed by Kundu (1993), the hydrostatic approximation becomes invalid above a frequency a few times $(Nf)^{1/2} \sim 1$ cph. It would be interesting to remove the hydrostatic approximation and calculate the internal wave response. The solution would be more difficult to compute because the eigenvalues become a function of frequency in addition to vertical mode number.

D'Asaro (1985) showed that over the course of a year, most of the forcing of near-inertial motions is contributed by a few dozen of the strongest intermittent storm events. On average, a few of these storm events occur each month. Such strong events are not necessarily well represented by an average wind stress spectrum, especially one patterned after the results of a handful of aircraft observations. We should keep in mind, however, that the dissipation time scale for internal waves is on the order of several months. Each individual storm event contributes only a small fraction to the local internal wave energy. An average wind stress spectrum might not be too bad an approximation, if one keeps in mind that it represents a long-term, large-area average.

There is additional evidence that supports the approach taken here. Garrett (1991) discussed results of Briscoe and Weller (1984) and Briscoe (1984), in which a lag of 2–3 months between internal wave energy levels and seasonal variations in wind stress was observed. In addition, the amplitude of variation in internal wave energy was about 40% of the amplitude in the seasonal wind stress variation. Garrett showed that these facts are consistent with an internal wave dissipation time scale of 100 to 200 days.

A question that arises is, Why is there a tendency toward universality, in the sense that seasonal variation in internal wave energy is weaker than seasonal wind stress variability? One possible explanation lies in the way that the efficiency of internal wave generation varies with mixed layer depth. Figure 8b shows how, as the mixed layer deepens, the coupling between the wind stress and the internal wave field becomes weaker. The internal wave spectral density varies approximately as h^{-1}. Because strong wintertime winds tend to be associated with a deeper mixed layer, there is a negative feedback mechanism that tends to reduce the variability in seasonal wind-induced internal wave variability.

It has long been known that wind forcing is a major generator of internal waves (e.g., Käse 1979). Several studies compute the frequency spectrum of internal waves in resonance with a particular wavenumber component of the wind field (Rubenstein 1983; Kundu 1993). As noted by Kundu (1993), these spectra are too spiky, as a result of modal resonances. In addition,

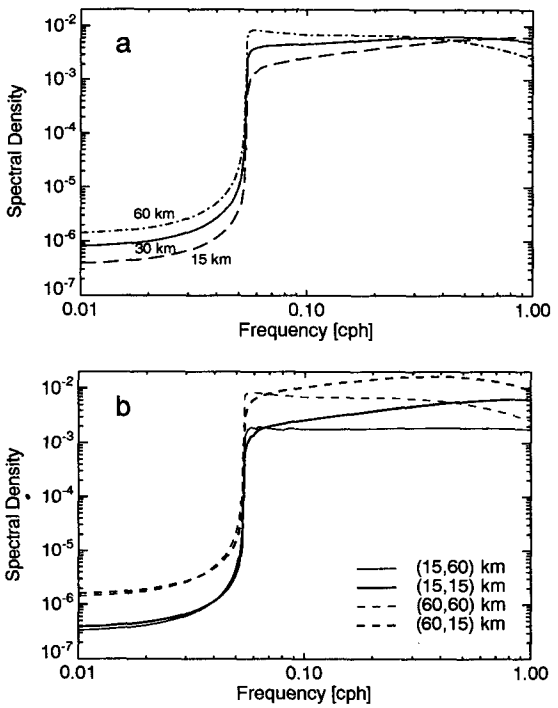

FIG. 11. Sensitivity of the wind-forced spectral density model of vertical velocity to variations in wind stress roll-off wavenumber components. (a) Roll-off wavenumbers $\beta_c = \beta_a = 2\pi/\lambda$, for $\lambda = 15$, 30, and 60 km. (b) Roll-off wavenumbers $(\beta_c, \beta_a) = (2\pi/\lambda_c, 2\pi/\lambda_a)$, for $(\lambda_c, \lambda_a) = (15, 60)$, (15, 15), (60, 60), and (60, 15) km.

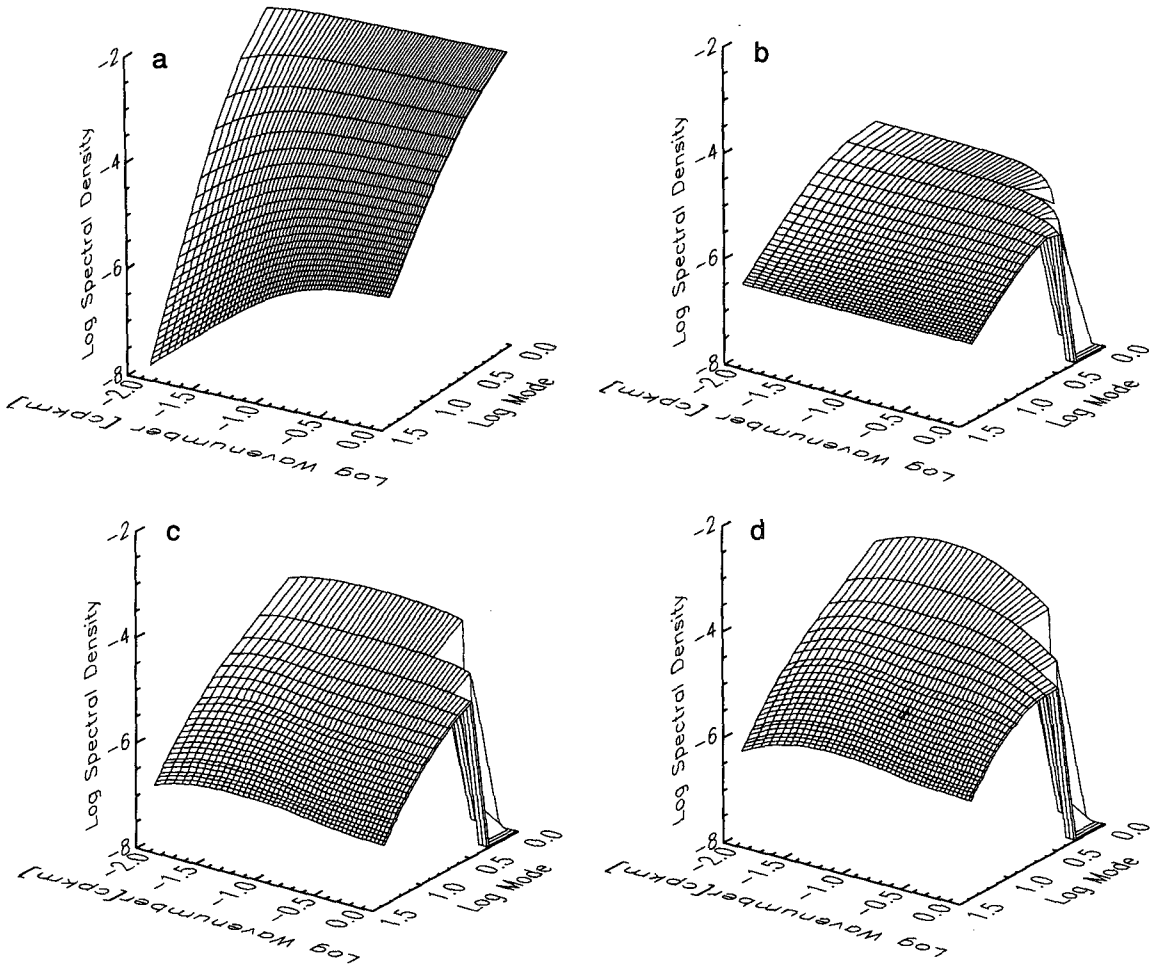

FIG. 12. Spectral density of vertical velocity, as a function of vertical mode number and horizontal wavenumber. (a) GM81 spectrum as function of total horizontal wavenumber, $\alpha = (k^2 + l^2)^{1/2}$. (b) GM81 spectrum as a function of one wavenumber component (e.g., l), where azimuthal isotropy is assumed. (c) Wind-forced model spectrum for wind stress roll-off wavelength components $(\lambda_c, \lambda_a) = (60, 30)$ km. (d) Wind-forced model spectrum for wind stress roll-off wavelength components $(\lambda_c, \lambda_a) = (90, 10)$ km.

the modeled spectral slope in the internal wave continuum is much steeper than that actually observed.

It is generally assumed that nonlinear interactions are responsible for the universal shape of the internal wave spectrum, and for the rapid relaxation of distorted spectra toward a universal form (Müller et al. 1986). These interactions could remove the spiky resonances and reduce the slope of the wind-forced internal wave spectrum, thus substantially modifying the spectrum into the observed universal spectrum. This present study provides evidence that the linear response to winds may be responsible for the first-order shape of the internal wave spectrum. Nonlinear interactions, although quite strong, need only make minor adjustments in order to "fine tune" the spectrum into its universal form.

Deviations from this universal form are observed only in special places, such as at the equator, under the polar ice cap, and so on. Deviations at the equator may be explained by the lack of the Coriolis force there. Deviations under the polar ice are not so simply explained. In light of the results of this paper, it seems likely that the stress applied at the ice–water interface has a different spectrum than that of mesoscale winds over the open ocean.

Levine (1990) computed frequency spectra from measurements of vertical displacement under the Arctic ice. He found the spectral slope to be nearly -1 rather than the -2 slope described by the GM81 model, which is primarily based on midlatitude observations. Moreover, the subice internal wave field was about 50 times less energetic than commonly observed at lower latitudes. We can speculate that the spectrum was primarily shaped by an ice-induced stress whose (i) divergence amplitude is much less than that of wind-induced stress in midlatitudes, and (ii) whose spectrum is much different from that of midlatitude wind stress. The resulting internal wave field, being much weaker

than in midlatitudes, is subject to weaker nonlinear interactions. Therefore, the ability of nonlinear interactions to reshape the internal wave spectrum is much reduced. As a result, we speculate that the observed spectrum more closely reflects the linear response to ice-induced stress than the effect of nonlinear interactions.

How might one test the hypotheses advanced in this paper against observations? This problem is made difficult in that internal waves can propagate long distances away from their region of origin, within a dissipation time scale. Perhaps the best approach is to relate long-term internal wave statistics to wind stress statistics. If an experimental site is chosen well away from continental boundaries and strong oceanographic fronts, then one might be justified in assuming local horizontal homogeneity of the wind stress statistics and the ocean environment.

A distributed set of meteorological buoys would be necessary to measure the mesoscale wind field. The model presented here predicts that energy in the internal wave continuum is most directly related to wind stress divergence. Therefore, one would want to compute the mesoscale divergence of the wind stress field, instead of simply the wind stress. An extensive mooring is required to measure internal waves over the entire water column. An array of moorings would allow one to examine the directionality of propagating internal waves.

Various statistical tests could be applied to study the coupling between the wind field and the internal wave field. The distribution of energy among vertical modes could be compared against those predicted by the present model. Frequency spectra of the modes could be compared against model predictions, such as those shown in Fig. 4. One could compute time-lagged correlations between wind stress divergence and internal wave energy. It might prove useful to try scaling the wind stress divergence by the mixed layer depth to see if the correlation is improved in accordance with model predictions. It would also be useful to compare statistics of directionality between internal waves and wind field propagation.

Acknowledgments. I gratefully acknowledge the support of the Physical Oceanography Program of the Office of Naval Research, Contract N00014-92-C-0098.

APPENDIX

GM81 Spectrum and Transformations

The Garrett and Munk (Munk 1981) spectral density of vertical velocity is described by

$$S_w^{GM}(\omega, n) = \frac{b^2 N_0}{N}(\omega^2 - f^2)E(\omega, n), \quad \text{(A1)}$$

where

$$E(\omega, n) = B(\omega)H(n)E; \quad E = 6.3 \times 10^{-5}, \quad \text{(A2)}$$

$$B(\omega) = \frac{2}{\pi}\frac{f}{\omega\sqrt{\omega^2 - f^2}}, \quad \text{(A3)}$$

$$H(n) = \frac{(n^2 + n_*^2)^{-1}}{\sum_{n=1}^{\infty}(n^2 + n_*^2)^{-1}}, \quad n_* = 3. \quad \text{(A4)}$$

Here the use of the GM superscript in (A1) serves to differentiate the GM81 spectrum from the wind-forced model spectrum. Through the use of the dispersion relation for hydrostatic internal waves,

$$\omega^2 = f^2 + \gamma^2\frac{\alpha^2}{n^2}, \quad \gamma = \frac{bN_0}{\pi}, \quad \text{(A5)}$$

we can transform the spectral density from $S_w^{GM}(\omega, n)$ to $S_w^{GM}(\alpha, n)$,

$$S_w^{GM}(\alpha, n) = \frac{b^2 N_0}{N}\frac{2f}{\pi}EH(n)\frac{\gamma^3\alpha^2}{n(f^2n^2 + \gamma^2\alpha^2)}. \quad \text{(A6)}$$

Here α is the total magnitude of the horizontal wavenumber vector,

$$\alpha = \sqrt{k^2 + l^2}. \quad \text{(A7)}$$

If we assume that the internal wave field is horizontally isotropic, then we are justified in applying the Abel transform,

$$S_w^{GM}(l, n) = 2\int_l^{\alpha_{max}} \frac{S_w^{GM}(\alpha, n)\alpha d\alpha}{\sqrt{\alpha^2 - l^2}}, \quad \text{(A8)}$$

and a similar transform to $S_w^{GM}(k, n)$. Here the upper limit of the integral is the maximum possible horizontal wavenumber, $\alpha_{max} = n\pi/b$. This integral can be solved analytically,

$$S_w^{GM}(l, n) = \frac{b^2 N_0}{N}\frac{4f}{\pi}EH(n)\left[\frac{\gamma}{n}\sqrt{\alpha_{max}^2 - l^2} - \frac{f^2 n}{\sqrt{f^2n^2 + \gamma^2\alpha_{max}^2}}\tan^{-1}\left(\frac{\gamma\sqrt{\alpha_{max}^2 - l^2}}{\sqrt{f^2n^2 + \gamma^2\alpha_{max}^2}}\right)\right]. \quad \text{(A9)}$$

Figures 12a and 12b show plots of (A6) and (A9), respectively.

REFERENCES

Briscoe, M. G., 1984: The monthly variability of upper-ocean internal wave energy: A progress report on the correspondence with wind stress. *Internal Gravity Waves and Small-Scale Turbulence: Proc.*, P. Muller and R. Pujalet, Eds., Hawaii Institute of Geophysics, 129–150.

——, and R. A. Weller, 1984: Preliminary results from the Long Term Upper Ocean Study (LOTUS). *Dyn. Atmos. Oceans*, **8**, 243–265.

Chave, A. D., D. S. Luther, and J. H. Filloux, 1991: Variability of the wind stress curl over the North Pacific: Implications for the oceanic response. *J. Geophys. Res.*, **96,** 18 361–18 379.

D'Asaro, E. A., 1985: The energy flux from the wind to near-inertial motions in the surface mixed layer. *J. Geophys. Res.*, **15,** 1043–1059.

——, 1989: The decay of wind-forced mixed layer inertial oscillations due to the β effect. *J. Geophys. Res.*, **94,** 2045–2056.

Eriksen, C. C., 1988: On wind forcing and observed oceanic wave number spectra. *J. Geophys. Res.*, **93,** 4985–4992.

Garrett, C., 1991: Paradigm lost? *Dynamics of Oceanic Internal Gravity Waves: Proc.*, P. Muller and D. Henderson, Eds., Department of Oceanography, University of Hawaii, 433–449.

Gill, A. E., 1984: On the behavior of internal waves in the wakes of storms. *J. Phys. Oceanogr.*, **14,** 1129–1151.

Gregg, M. C., 1984: Persistent turbulent mixing and near-inertial internal waves. *Internal Gravity Waves and Small-Scale Turbulence: Proc.*, P. Muller and R. Pujalet, Eds., Hawaii Institute of Geophysics, 1–24.

——, E. A. D'Asaro, T. J. Shay, and N. Larson, 1986: Observations of persistent mixing and near-inertial internal waves. *J. Phys. Oceanogr.*, **16,** 856–885.

Käse, R. H., 1979: Calculations of the energy transfer by the wind to near-inertial internal waves. *Deep-Sea Res.*, **26,** 227–232.

Kundu, P. K., 1976: An analysis of inertial oscillations observed near Oregon coast. *J. Phys. Oceanogr.*, **6,** 879–893.

——, 1993: On internal waves generated by traveling wind. *J. Fluid Mech.*, **254,** 529–560.

——, and R. E. Thomson, 1985: Inertial oscillations due to a moving front. *J. Phys. Oceanogr.*, **15,** 1076–1084.

Levine, M. D., 1990: Internal waves under the Arctic pack ice during the Arctic internal wave experiment: The coherence structure. *J. Geophys. Res.*, **95,** 7347–7357.

Müller, P., G. Holloway, F. Henyey, and N. Pomphrey, 1986: Nonlinear interactions among internal gravity waves. *Rev. Geophys.*, **24,** 493–536.

Munk, W., 1981: Internal waves and small-scale processes. *Evolution of Physical Oceanography*, B. A. Warren, C. Wunsch, Eds., The MIT Press, 264–291.

Orlanski, I., 1975: A rational subdivision of scales for atmospheric processes. *Bull. Amer. Meteor. Soc.*, **56,** 527–530.

Overland, J. E., and J. G. Wilson, 1984: Mesoscale variability in marine winds at mid-latitude. *J. Geophys. Res.*, **89,** 10 599–10 614.

Pollard, R. T., and R. C. Millard, 1970: Comparison between observed and simulated wind-generated inertial oscillations. *Deep-Sea Res.*, **17,** 813–821.

Rubenstein, D., 1983: Vertical dispersion of inertial waves in the upper ocean. *J. Geophys. Res.*, **88,** 4368–4380.

Sanford, T. B., 1991: Spatial structure of thermocline and abyssal internal waves. *Dynamics of Oceanic Internal Gravity Waves: Proc.*, P. Muller, D. Henderson, Eds., Department of Oceanography, University of Hawaii, 109–141.

Weller, R. A., and D. Halpern, 1983: The velocity structure of the upper ocean in the presence of surface forcing and mesoscale oceanic eddies. *Phil. Trans. Roy. Soc. London A*, **308,** 327–340.

Willebrand, J., S. G. H. Philander, and R. C. Pacanowski, 1980: The oceanic response to large-scale atmospheric disturbances. *J. Phys. Oceanogr.*, **10,** 411–429.